Journal of Materials Chemistry A

Single-Step Exfoliation of Black Phosphorus and Deposition of Phosphorene via Bipolar Electrochemistry for Capacitive Energy Storage Application

Journal:	*Journal of Materials Chemistry A*
Manuscript ID	TA-ART-09-2019-009641.R1
Article Type:	Paper
Date Submitted by the Author:	09-Oct-2019
Complete List of Authors:	Rabiei Baboukani, Amin; Florida International University, Department of Mechanical and Materials Engineering Khakpour, Iman; Florida International University College of Engineering and Computing, mechanical and Materials Engineering fiu Drozd, Vadym; Florida International University, Mechanical and Materials Engineering Allagui, Anis; University of Sharjah, Sustainable and Renewable Energy Wang, Chunlei; Florida International University, Department of Mechanical and Materials Engineering

ARTICLE

Single-Step Exfoliation of Black Phosphorus and Deposition of Phosphorene via Bipolar Electrochemistry for Capacitive Energy Storage Application

Received 00th January 20xx,
Accepted 00th January 20xx

DOI: 10.1039/x0xx00000x

Amin Rabiei Baboukani[a], Iman Khakpour[a], Vadym Drozd[a,b], Anis Allagui[c], and Chunlei Wang[a,b*]

Black phosphorus (BP) is a two-dimensional material that has gained attention for various applications due to its exceptional physical and chemical properties such as tunable bandgap and high charge carrier mobility. However, the critical step towards the application of BP is still contingent on successfully exfoliating the bulk material into a few-layer phosphorene nanosheets. Herein, we show a one-step, facile, and environmentally-friendly method of bipolar exfoliation-and-deposition of BP nanosheets on a positive feeding electrode. The exfoliated-and-deposited materials are high-quality phosphorene with orthorhombic crystal structure, and are adherent onto the substrate in a fractal and structured morphology. The electrochemical performance of the material was evaluated in a symmetric, two-electrode configuration soaked in aqueous electrolyte for capacitive energy storage application. The results revealed a fractional-order capacitive behaviour in the low-to-medium frequency, and a high stability and reversibility for at least 40000 cycles. The power performance is outstanding with 1.4 mW cm^{-2} at a constant current rate of 0.5 mA cm^{-2}, which is superior than most of the 2D materials-based devices such as MXene, 2D MnO_2, graphene or graphene oxide.

Introduction

Alongside with graphene and its fascinating properties [1], other two-dimensional (2D) materials, such as transition metal oxides [2], layered transition metal dichalcogenides (TMDs) [3], and boron nitride [4] have stimulated significant research interest for next-generation electronic and optoelectronic devices because of their outstanding structural and physical properties [5-7]. Among all 2D materials, graphene has the highest charge carrier mobility (up to 100,000 $cm^2 V^{-1} s^{-1}$), but its zero bandgap prohibits its operation as a semiconducting material in electronic applications [8, 9]. Molybdenum disulphide presents a remarkable bandgap but suffers from limited carrier mobility [10]. Recently, black phosphorus (BP), which was discovered by Bridgman back in 1914 [11], has recaptured attention due to its promising physical and chemical properties [12-14]. In terms of structure, which is similar to graphite, strong P-P covalent bonds in each layer of BP form a puckered honeycomb structure, and neighbouring layered BP nanosheet (known as a phosphorene) adhered together with a weak van der Waals interlayer interactions (see Figure 1S) [15]. BP is a p-type semiconductor which shows a tuneable direct bandgap in a desirable range from 0.3 eV for bulk to 2.0 eV for a few-layer BP [16, 17], high carrier mobility (up to 1000 $cm^2 V^{-1} s^{-1}$)[18], and acceptable mechanical flexibility compared to the other 2D materials [19]. Furthermore, BP is the most stable allotrope of phosphorus compared to the white phosphorus and red phosphorus (RP) [20]. These exclusive properties suggest the possible usage of phosphorene in nanoelectronics and optical devices. Additionally, due to its high surface area and high theoretical capacity, phosphorene is viewed as a great candidate for electrochemical energy storage devices, such as batteries and supercapacitors [21, 22].

According to theoretical studies and experimental characterizations [23], the real application of BP depends on the method of preparation and exfoliation of few-layer phosphorene from the bulk material [24]. To date, different top-down and bottom-up approaches have been used to prepare phosphorene nanosheets. The top-down processes are more common and rely on chemically or mechanically weakening and breaking the interlayer interactions, while the bottom-up techniques are based on chemical synthesis from phosphorus precursors [25]. Smith et al. synthesized a few-layer phosphorene films of 3.4 to 600 nm thickness on a silicon substrate through the bottom-up chemical vapour deposition (CVD) method using RP as a starting material [26]. Besides CVD, there are limited bottom-up synthesis methods due to the lack of suitable precursors and the associated high costs of preparation [27]. Top-down methods are mostly used for the formation of phosphorene based on mechanical and liquid exfoliation of BP. The well-known Scotch tape method of micromechanical cleavage was applied by Li et al. to exfoliate and fabricate phosphorene on SiO_2/Si substrate [28]. However, this method suffers from low yield and poor scalability. As an alternative, liquid-phase exfoliation revealed promising results for BP exfoliation. It consists of the dispersion of BP in a

[a] Department of Mechanical and Materials Engineering, Florida International University, Miami, FL33174, USA
[b] *Center for the Study of Matter of Extreme Conditions (CeSMEC), Florida International University, Miami, FL 33199, USA*
[c] *Department of Sustainable and Renewable Energy Engineering, University of Sharjah, Sharjah, UAE*
** Corresponding authors (wangc@fiu.edu).*

† Footnotes relating to the title and/or authors should appear here.
Electronic Supplementary Information (ESI) available: [details of any supplementary information available should be included here]. See DOI: 10.1039/x0xx00000x

solvent (deionized (DI) water or organic/inorganic solutions), sonication, and centrifugation of the exfoliated materials [29, 30]. Brent et al. obtained two layers of phosphorene using a one-step ultrasonication of BP in N-methylpyrrolidone (NMP) solution [31]. By controlling the sonication power and centrifuge speed of rotation, large quantities and to a certain extent controllable size of phosphorene nanosheets (a few nanometres to several tens of micrometres) have been produced, which makes this method more favourable compared to the mechanical exfoliation [32, 33]. Yasaei et al. used dimethylformamide (DMF) and dimethyl sulfoxide (DMSO) as a stripping solvent to synthesize large scale and highly crystalline phosphorene nanosheets with the thickness of 11 nm [34]. Isopropyl alcohol (IPA) [35], ionic liquids [36] and N-cyclohexyl-2-pyrrolidone (CHP) [37] were also reported as solvents for liquid exfoliation of BP. Very recently, Yan et al. developed a simple solvothermal-assisted exfoliation method with acetonitrile as a solvent to synthesize a few-layer phosphorene within a size range up to 10 µm. Acetonitrile was shown to weaken the van der Waals bonds and decrease the sonication time [38]. However, the use of hazardous solvents and the high concentration of structural defects in the final products remain the major disadvantages of liquid exfoliation methods, which may limit their widespread adoption. Electrochemical exfoliation is another liquid-based exfoliation technique to prepare a few-layer phosphorene that is faster, inexpensive and more tractable [39]. In this method, the exfoliation occurs in organic or aqueous solutions by applying a fixed voltage between the bulk BP and an inert platinum electrode [40, 41]. Li et al. successfully synthesized highly crystalline phosphorene nanosheets using BP as a cathode in a nonaqueous electrolyte (0.01 M tetraalkylammonium salt in DMSO) and by applying a cathodic voltage of -5 V [42]. Ambrosi et al. used 0.5 mol l^{-1} H_2SO_4 solution and a BP anode. First, they applied 1 V to the bulk BP to initiate the intercalation of the electrolyte anions and then 3 V for the exfoliation process [43]. Although the electrochemical exfoliation methods can successfully exfoliate bulk BP into phosphorene, they are nonetheless multi-step and time-consuming procedures, and thus less attractive for practical applications. It is therefore necessary to develop alternative techniques that can fabricate a few-layer BP-modified substrate in a facile, single-step, scalable, and eco-friendly manner.

In this study, we propose a novel and straightforward two-in-one process to exfoliate BP into phosphorene nanosheets in DI water, which are then dragged electrophoretically to be deposited on a conductive substrate. The procedure is based on the mechanism of bipolar electrochemistry (BPE). BPE is a well-known technique since 1960s which is based on applying a sufficiently high voltage to generate electrochemical reactions between two feeding electrodes and a conductive bipolar electrode placed wirelessly between them [44]. The difference in the electric potential between the solution and the bipolar electrode drive redox reactions on the cathodic and anodic poles of the bipolar electrode [45]. This method has been used for different applications such as electronic devices manufacturing, electrochemical sensing, and optical detection due to its low cost, user-friendly, and high-efficient operation [46, 47]. It has been recently used for the simultaneous exfoliation of graphene from graphite and its deposition on stainless steel feeding electrode [48-50]. As mentioned earlier, liquid-based exfoliation of BP is mainly conducted in organic solvents that are adsorbed by the surface of exfoliated BP and are very difficult to be removed later. Here, we use DI water as a solvent for the exfoliation of BP, which makes this technique cost-effective and environmental-friendly. The exfoliated-and-deposited BP nanosheets were characterized morphologically, optically and chemically using scanning electron microscopy (SEM), transmission electron microscopy (TEM), Raman spectroscopy and X-ray photoelectron spectroscopy (XPS). The electrochemical characterization of the phosphorene-modified positive feeding electrode showed a fractional-order capacitive behaviour with discharge energy of 22.8 nW.h cm^{-2} recoverable with very high efficiency after 10000s of charge/discharge cycles. Fractional-order capacitors or constant phase elements (CPE) have an impedance of the form $Z(s) = 1/s^{\alpha}C_{\alpha}$, $(0<\alpha<1)$ and constant impedance phase angle $\phi(Z) = -\alpha\pi/2$ independently of the frequency, which is suitable for instance for oscillator circuits for timing applications, filters for frequency selectivity purposes, and in fractional-order proportional–integral–derivative controllers.

Experimental

Materials and methods

Two 316 stainless steel electrodes (1×4 cm^2) serving as positive and negative feeding electrodes were placed vertically in in DI water (18 MΩ·cm resistivity) at a distance of 3 cm from each other (see BPE cell in Figure 1). A 1 cm long and 2.5 mm in diameter bulk poly-crystalline BP bar (99.998% purity, supplied by Smart-Elements, Germany) was placed wirelessly between the two feeding electrodes. A multi-channel DC Power Analyzer (Agilent Technologies N6705A) was used to drive the BPE process, which was conducted with 30 Vdc (i.e. electric field of 10 V cm^{-1}) for continuous 24 hours at ambient conditions.

Materials characterization

The microstructural and morphological properties of the exfoliated BP were characterized by field-emission scanning electron microscopy (JEOL FESEM 7000) and field-emission transmission electron microscopy (Tecnai TF 20 TEM). High-resolution TEM (HRTEM) with selected-area electron diffraction (SAED) were conducted at an accelerating voltage of 200 kV, and the field emission gun with a resolution of 2 Å. Focused Ion Beam (Quanta 3D; Dual Beam) was used for the TEM sample preparation. The Raman spectra were collected on a BaySpec Raman spectrometer using a 514-nm laser excitation. The chemical composition of the exfoliated-and-deposited phosphorene on the stainless steel substrates was evaluated using X-ray photoelectron spectroscopy (XPS) on a Physical Electronics 5400 ESCA instrument with Al Kα radiation (1486.6 eV).

Electrochemical characterization

The electrochemical measurements were performed on a VMP3 Bio-Logic potentiostat. Two symmetric positive feeding electrodes (after BP exfoliation) of 0.5×0.5 cm^2 were assembled in a Swagelok electrochemical cell using 1 mol l^{-1} Na_2SO_4 solution and Celgards 2400 microporous polypropylene separator. The spectral impedance of the device was measured at 0 Vdc with 10 mV ac perturbations from 1 MHz down to 10 mHz. The cyclic voltammetry (CV) tests at the scan rates of 2 to 1000 mV s^{-1} and galvanostatic charge/discharge (GCD) at different current densities from 25 to 500 µA cm^{-2} were carried out over the voltage range of 0 to 0.7 V.

Results and discussion

The BPE setup used to exfoliate-and-deposit phosphorene nanosheets starting from bulk BP is shown in Figure 1. In brief, a BP bar was placed wirelessly in the centre of the cell pre-filled with DI water, and two stainless steel feeding electrodes were placed at a distance of 3 cm apart. Figure 2S which shows typical SEM images of the bulk BP before exfoliation consisting of an angular, closely-stacked and layered structure. Due to the concept of bipolar electrochemistry, in general the induced voltage on the two pole of bulk BP depends on the applied voltage, length of BP electrode, and distance between two feeding electrodes. By applying higher voltage, using longer bulk BP and decreasing distance between two feeding

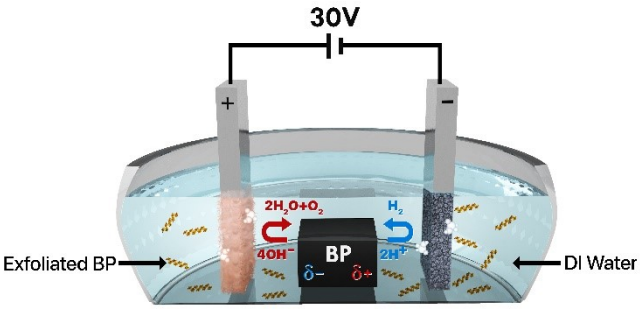

Fig 1 Schematic illustration of the two-in-one bipolar electrochemical cell used for (i) BP exfoliation into phosphorene, and (ii) subsequent electrophoretical deposition of the suspended phosphorene on the feeding electrodes.

electrodes, the induced voltage will increase. The typical electric field was reported as around 5 to 15 Vcm^{-1} for successful BPE exfoliation of graphite [48-51]. In this study, cell voltage of 30 V was selected based on the electric field of 10 Vcm^{-1}. The extremities of the BP substrate across the direction of the electric field get polarized in the opposite polarity to the feeding electrodes resulting in the wireless compartmentalization of the BP into anodic and cathodic poles [46]. The bulk BP remains almost isopotential during BPE. When the bipolar potential is large enough hydrogen and oxygen bubbles were generated at the surface of the negative and positive poles of bulk BP, respectively, as a result of water electrolysis reaction, and can be easily visualized (Supplementary Video 1). Given the "crumbly" and layered nature of the bulk BP bar, H^+ and OH^- ions generated during the water decomposition can be intercalated to the bulk BP and overcome the weak van der Waals forces of BP layers. Therefore, 2D phosphorene particles can be detached and exfoliated from the bulk BP. Due to the Vdc electrophoresis phenomena, 2D phosphorene nanosheets will be transported and deposited on to the feeding electrode. Figure 3S shows the change of the cell current versus time during the exfoliation process. It is clear that the current progressively increased with the time as a result of increased conductivity of the solution, which can be attributed to the collective effect of water electrolysis and by-products from BP exfoliation.

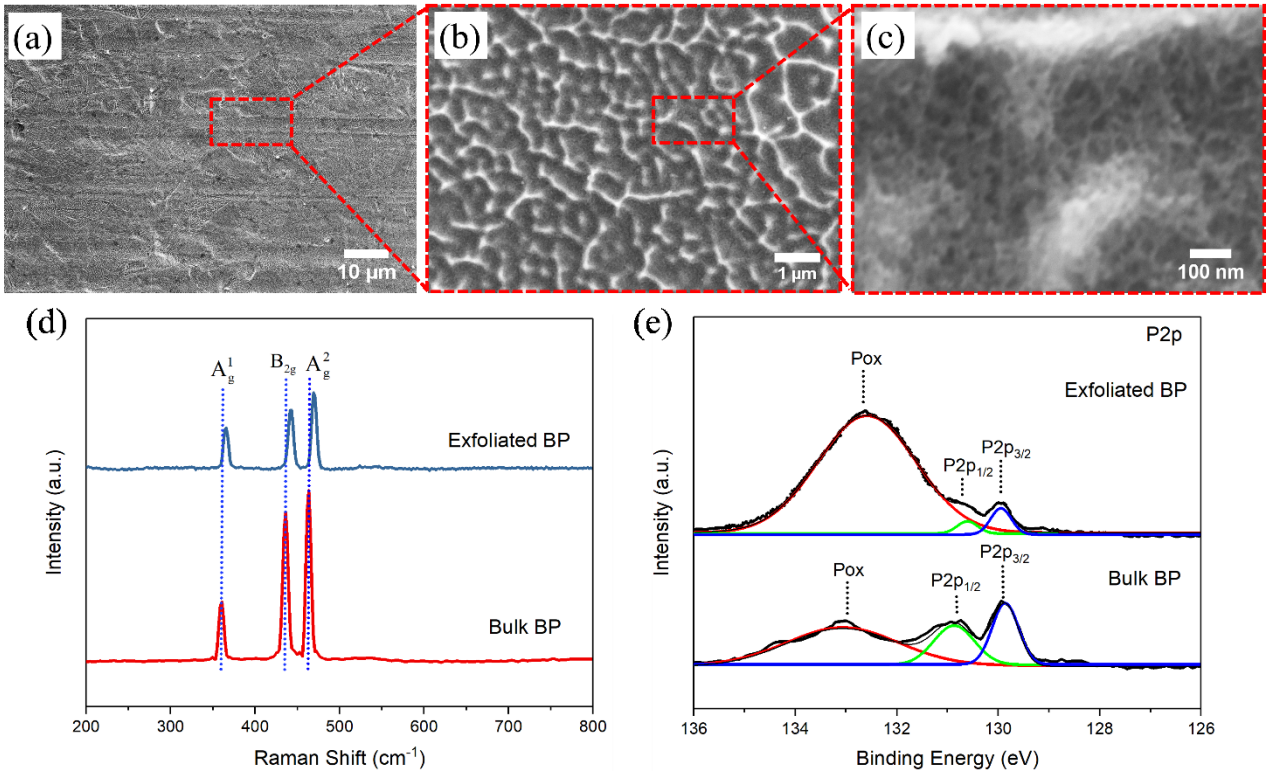

Fig 2 (a-c) Typical SEM images of exfoliated and deposited black phosphorus nanosheets on the positive electrode in different magnification. (d) Raman spectra, and (e) XPS spectra of the BP crystal and bipolar exfoliated-and-deposited BP nanosheets.

After 24 hours of BPE, the bulk BP did not show any noticeable change, however, obvious deposition of a thin film on the positive electrode of the bipolar cell can be observed. It should be noted that in our recent study of graphene exfoliation via BPE [50], deposition occurs on both positive and negative feeding electrodes. More detailed study needs to be done to investigate the possible deposition of phosphorene on the negative feeding electrode.

Typical SEM micrographs of the positive feeding electrode after 24 hours of operation are shown in Figure 2 (a-c) at different magnifications. One can observe a homogeneous distribution of thin phosphorene nanosheets on the substrate with a structured and fractal structure. The Raman spectroscopy results of the same feeding electrode are shown in Figure 2(d) along with the Raman spectrum of the bulk BP for comparison. From the six theoretical Raman vibration modes of black phosphorus, three prominent peaks appear in the range from 300 cm^{-1} to 500 cm^{-1} [52, 53] which confirms that the BP exfoliation/deposition was successful. These peaks are A_g^1 (out of plane), B_{2g}, and A_g^2 (in-plane) vibration modes at 361 cm^{-1}, 439 cm^{-1}, and 467 cm^{-1}, respectively, indicating good agreement with previous results [54-56]. For the exfoliated BP, compared to the bulk BP, blue-shifts by about 3.1 cm^{-1}, 7.0 cm^{-1}, and 5.7 cm^{-1} can be observed for the Raman modes A_g^1, B_{2g}, and A_g^2, respectively. These shifts may be associated with the less hindered vibration of the phosphorus atoms due to the weakened interlayer van der Waals forces [30, 37]. The observed blue shifts for the exfoliated BP confirm the reduction in the number of BP layers. It is also clear that due to the reduction of BP thickness, the intensity of the three bands decreased significantly for the phosphorene nanosheets [57-59]. The number of phosphorene layers after exfoliation could be estimated as 3 to 5 layers based on the intensity ratio of 2.75 for the A_g^2 / A_g^1 vibration modes [60].

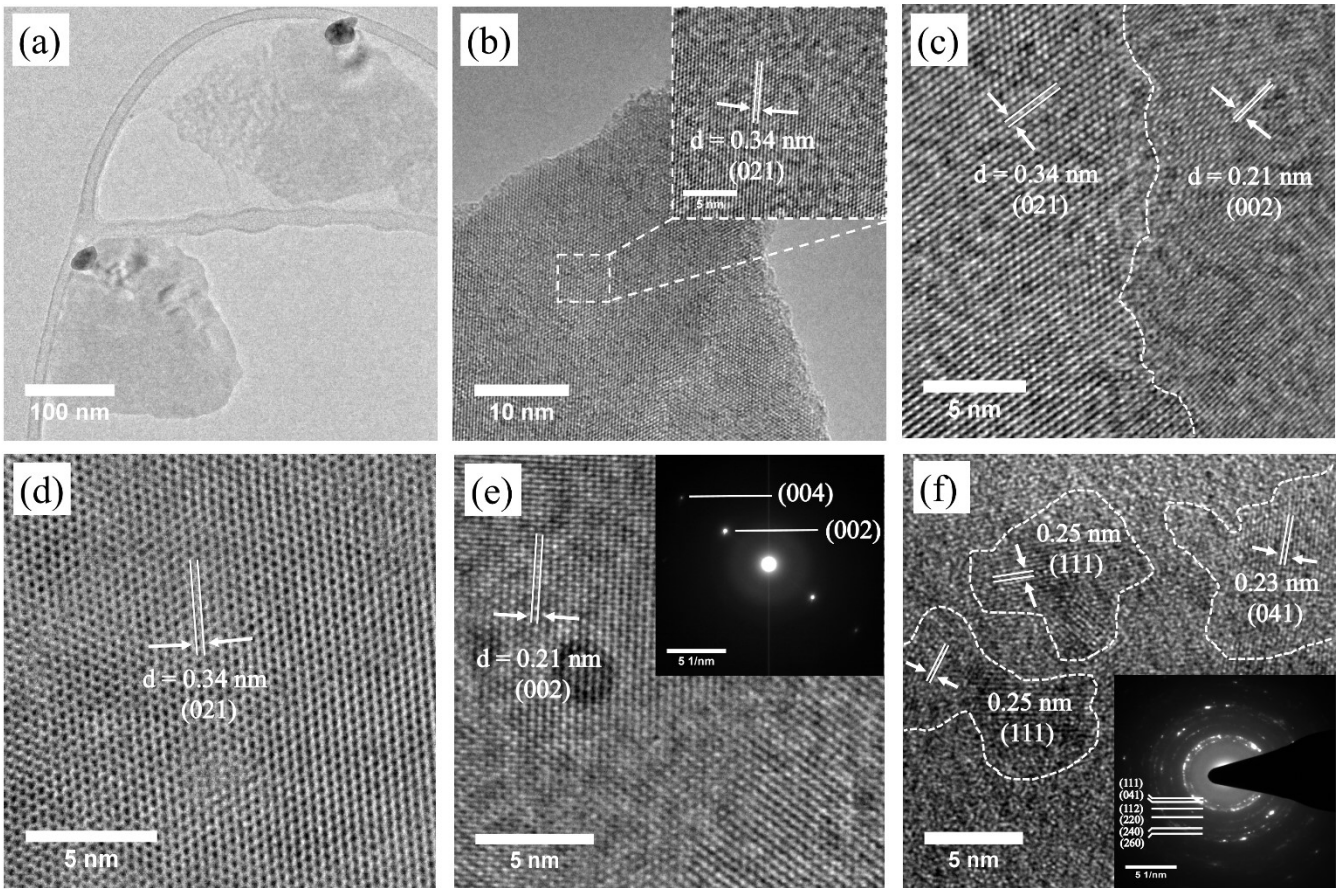

Fig. 3 (a) Typical low-magnification TEM image of the BP nanosheets. (b-f) HRTEM images of exfoliated BP nanosheets. The insets of (e,f) are the SAED patterns of exfoliated BP nanosheets.

XPS spectra of the bulk BP and exfoliated BP nanosheets (Figure 2(e)) revealed two well-defined $P2P_{1/2}$ and $P2P_{3/2}$ components at a binding energy of about 130.8 eV and 129.8 eV, respectively, which are related to the crystalline black phosphorus peaks. A broad peak can be observed at around 133.0 eV and 132.8 eV for bulk BP and exfoliated BP nanosheets, respectively, which could be assigned to phosphorus-oxygen bond (POx) [61]. The POx bond can be attributed to the high reactivity of BP and spontaneous formation of surface oxide layer in air [43]. The XPS spectrum of the exfoliated phosphorene on the stainless steel show less intense POx peak compared to the bulk BP indicating that the bipolar exfoliated phosphorene has higher degree of oxidation because high surface area phosphorene nanosheets are more reactive and sensitive to oxygen. The peak shifts for the POx, $P2P_{1/2}$and $P2P_{3/2}$ are around 0.3, 0.2, and 0.09 eV to the lower values, respectively. The peaks shift to the lower binding energies could be attributed to the reduced number of layers of BP nanosheets after bipolar exfoliation [62, 63].

In order to investigate the morphology of the exfoliated BP nanosheets as well as the crystalline quality, TEM characterization was carried out. The TEM images of the exfoliated BP nanosheets collected from the DI water after the 24-hour BPE operation are shown in Figure 3 (a-f). Figure 3 (a), shows a low-resolution TEM image of electron-transparent, thin phosphorene nanosheets with lateral size in the range of a few hundreds of nanometres which demonstrate the successful exfoliation of BP by bipolar electrochemistry method [43, 64]. HRTEM images confirming the crystallinity of the phosphorene are shown in Figure 3 (b-f). The interplanar distances and corresponding Miller indices of the BP nanosheets are labelled on the HRTEM images. It is clear from Figure 3 (b-f) that the orthorhombic crystal structure of BP appears to be not affected by the bipolar exfoliation, which confirms a low defect concentration in produced phosphorene nanosheets. The exfoliated BP nanosheets revealed different lattice fringes with interplanar distances of 0.34, 0.21, 0.23, and 0.25 nm, which could be assigned to the (021), (002), (041), and (111) atomic planes of orthorhombic black phosphorus, respectively. From SAED pattern presented in the insets of Figure 3 (e, f), the orthorhombic single crystals of the exfoliated BP is confirmed which is in good agreement with previous reports [36, 65]. The possible reason for various size of crystalline domains of phosphorene nanosheets after bipolar exfoliation could be due to the poly-crystalline nature of the bulk BP. The interplanar distances are matched with the d-spacing of orthorhombic black phosphorus (JCPDS No 96-101-0326).

Finally, owing to the structured surface of the exfoliated-and-deposited phosphorene nanosheets, the electrochemical performance of the positive feeding electrode was evaluated for capacitive energy storage application in a two-electrode symmetric configuration. We first analysed the open-circuit spectral impedance of the device which was measured with 10 mV ac amplitude excitations from 1 MHz down to 10 mHz. The Nyquist plot and Bode plot (inset) are depicted in Figure 4(a). The spectral phase is relatively constant at an average of -66.5 deg. in the low-to-medium frequencies (less than 1000 Hz) and heads towards the resistive, and then inductive behaviour as the frequency is increased. The non-ideal behaviour can be attributed to the crystalline inhomogeneity and surface roughness of the electrode. Such non-ideality can be modelled using the fractional-order Randles model (see inset in Figure 4(a)) of impedance:

$$Z(j\omega) = R_s + \frac{R_p}{R_p C_\alpha (j\omega)^\alpha + 1} \quad (1)$$

The model includes a series resistance R_s, a parallel resistance R_p, and a constant phase element (CPE) of impedance proportional to $1/(j\omega)^\alpha$ ($Z_{CPE} = 1/C_\alpha(j\omega)^\alpha$ where C_α is the CPE parameter and α is a dispersion coefficient that can take values between 0 and 1) [66]. Using nonlinear least square fitting (Figure 4(a) in dashed line), the value of R_s was found to be 3.135 Ω, R_p = 251 kΩ, C_α = 0.103 mF $s^{-0.261}$, and α = 0.739. In the time domain, this non-ideal behaviour can be viewed as a fractional differentiation of order α performed by the capacitive part of the device, i.e. $i(t) = C_\alpha d^\alpha v(t)/dt^\alpha$ [67-69]. This is different from the first-order differentiation $i(t) = Cdv(t)/dt$ known for ideal capacitors, and can find application in fractional-order PID controllers [70], impedance matching circuits [71], filters [72], etc.

A particular output of the fractional differentiation operation of the device is its response to a step function. For a step current input (i.e. $i(t) = 0$ for $t < 0$, and $i(t) = I_{cc}$ for $t \geq 0$), and given that $R_p \gg R_s$, the voltage-time response is actually proportional to a power law function and not a linear function, such that [69]:

$$v(t) = V_0 + I_{cc}\left[R_s + \frac{t^\alpha}{C_\alpha \Gamma(1+\alpha)}\right] \quad (2)$$

Here V_0 is the initial voltage on the device and $\Gamma(\cdot)$ is the

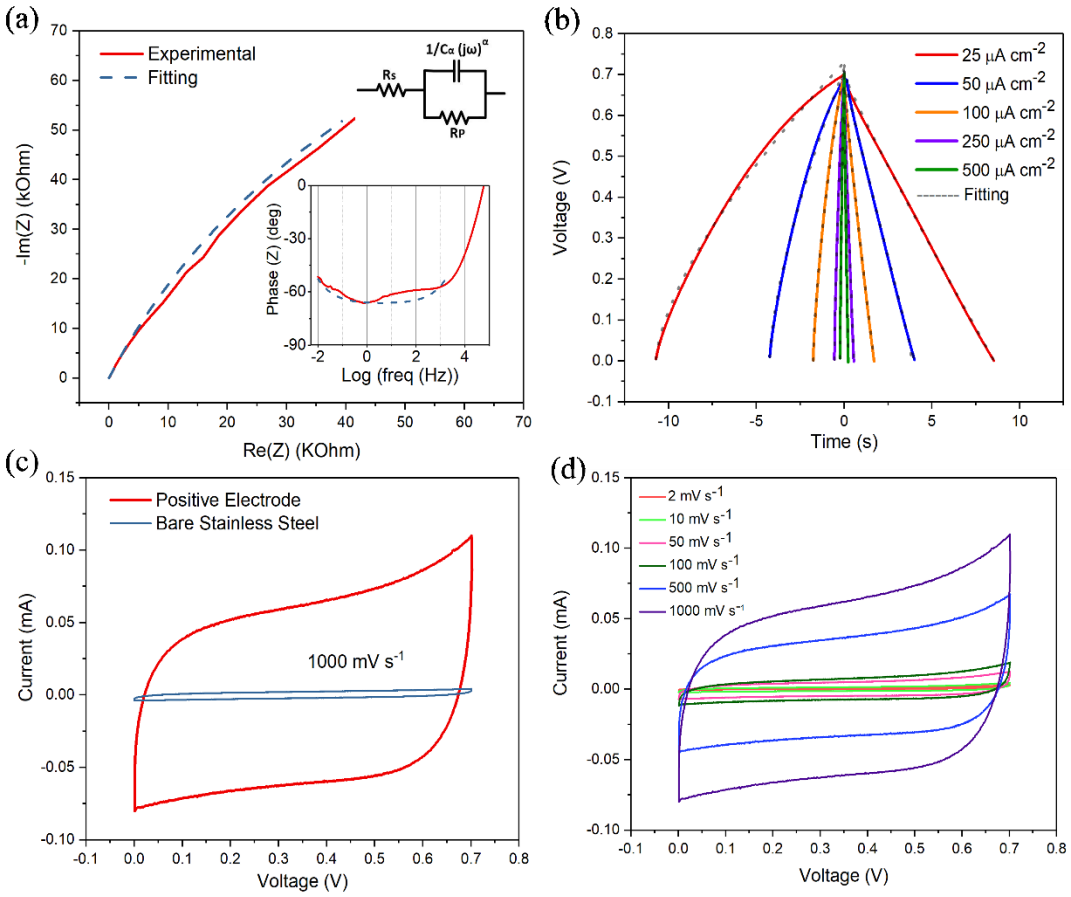

Fig 4 Electrochemical characterization results of positive feeding electrode-based device: (a) Complex-plane representation of real versus imaginary parts of impedance; the inset shows the impedance phase angle plot versus frequency and circuit of the fractional-order Randles model. (b) Voltage-time profiles resulting from constant-current charging/discharging measurements. (c) Cyclic voltammetry profile compared to that of a bare stainless steel-based device at the same voltage scan rate of 1000 mVs^{-1}. (d) Cyclic voltammetry profiles at different scan rates.

Gamma function. The same can be adapted to a step decrease using −Icc which results in a power law decrease [73]. In Figure 4(b) we show the resulting voltage-time profiles in response to GCD tests with different values of I_{cc} from 25 to 500 μA cm^{-2}. Using discrete Fourier decomposition, these responses correspond to fundamental frequencies from about 50 mHz to 1 Hz. At low current rates, it is clear that the device voltage discharge is relatively linear with negligible low Ohmic drop. However, a clear transition from linear to nonlinear, power law voltage-time relationship can be observed as the current charging/discharging is increased. Nonlinear least-squares fitting of the experimental discharge data using Equation 2 (Figure 4(b) in dashed lines) resulted in the values of the dispersion coefficient α being 0.927, 0.978, 0.844, 0.800 and 0.759 and those of C_α being 0.188, 0.210, 0.224, 0.259 and 0.297 mF s$^{\alpha-1}$ for the discharge currents 25, 50, 100, 250 and 500 μA cm^{-2}, respectively. The values of α for the five corresponding charging waveforms were found to be practically constant with an average of 0.674 and a small standard deviation of 0.008, with C_α being 0.268, 0.282, 0.237, 0.236 and 0.253 mF s$^{\alpha-1}$. The variation in the values of α in these cases is actually a characteristic feature of fractional-order capacitive devices. Contrary to ideal capacitors, these devices possess an inherent memory effect that makes their response sensitive to the type and form of the applied excitation [74], as well as to the pathway they followed to reach a given state [67]. The same applies to the different parameters values extracted from the EIS modelling at which the device is perturbed with small signals around its equilibrium state (open-circuit voltage), whereas with the square wave currents, the device is operating in dynamic mode.

For the sake of comparison, it is convenient to define, with caution, an effective capacitance $C_{eff} = C_\alpha\Gamma(1+\alpha)t^{1-\alpha}$ in units of Farads that combines both parameters α and C_α and this by equating the term $t^\alpha/C_\alpha\Gamma(1+\alpha)$ in equation (2) with t/C_{eff} as if

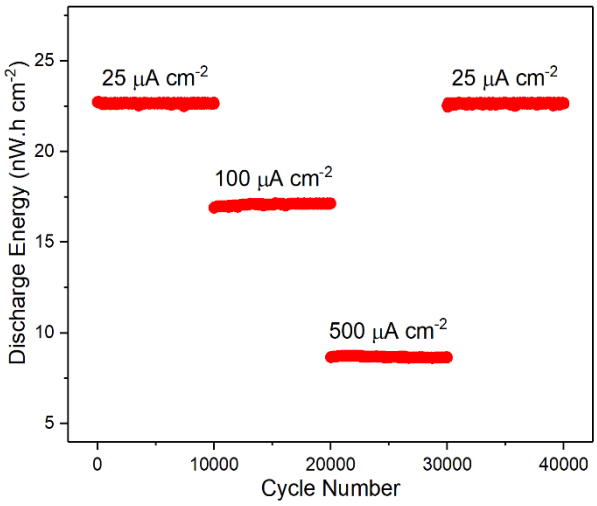

Fig 5 Discharge energy vs. cycle number measured at different currents of the exfoliated-and-deposited phosphorene on the positive electrode.

the device is an ideal capacitor (i.e. α =1) [69]. The values of C_{eff} computed for the charging/discharging sequences at the increasing currents ±25, ±50, ±100, ±250 and ±500 μA cm^{-2} were found to be decreasing as expected, i.e. 0.369, 0.300, 0.244, 0.194 and 0.165 mF, and 0.305, 0.288, 0.243, 0.196 and 0.164 mF, respectively. The difference between the two sets of values, especially at low rates, can be attributed to possible electrochemical irreversibility, increased resistive behavior of the device (see Bode plot in inset of Figure 4(a) in the low-frequency window), as well as the fact that parameters of fractional-order devices are dependent on the integral past history of the device

The dynamic performance of the device was then characterized using CV test. Figure 4 (c) shows the current-voltage response of the phosphorene-based device recorded at the scan rate of 1000 mV s^{-1} compared to that of a bare stainless steel-based device. Clearly, the phosphorene coating exhibits a capacitive electrical energy storage capability. In Figure 4 (d), the performance of the device was measured at different voltage scan rates (2 to 1000 mV s^{-1}). The voltammograms get wider with the increase of scan rate. The curves are nearly rectangular without any noticeable peaks belongs to reversible redox reactions, implying the storage mechanism of the device based on double-layer charge storage. (this do not exclude completely the existence of some parasitic redox reaction that may take place).

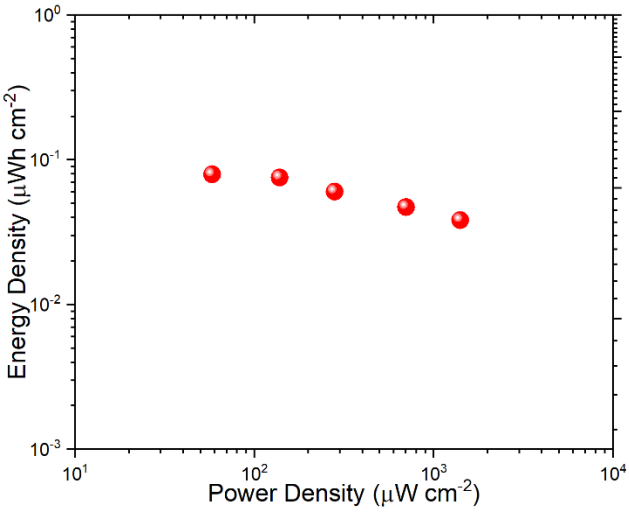

Fig 6 Ragone plot of energy density vs. power density at different currents from 25 to 500 μA cm^{-2} of the exfoliated-and-deposited phosphorene on the positive electrode.

We also evaluated the electrochemical stability of the device. Figure 5 shows the results of its rate capability performance computed from tests conducted at different constant charging/discharging currents for 40000 successive cycles. The plot shows the discharged energy vs. cycle number which is directly computed from the time-integral of the instantaneous

power, i.e. $e(t) = \int p(t)dt$ with $p(t)= i(t).v(t)$, and not from the computation of the capacitance which, again, can be ambiguous to define for this case given the fractional-order nature of the device. The discharge energy of the electrode with area of 0.5 cm^2 prepared by BPE method provides 22.8 nW.h cm^{-2} for a constant current density of 25 µA cm^{-2}. The flatness of the curves for the different applied currents demonstrates the superior stability and reliability of the phosphorene electrodes used for the fabrication of the device. Furthermore, the recovery of the same discharge energy for I_{cc} = 25 µA cm^{-2} after 30000 charge/discharge cycles is clear an evidence of its excellent reversibility and long-term stability.

The delivered energy density vs. power density computed from the response of the device at different discharge currents from 25 to 500 µA cm^{-2} are plotted in Figure 6. Again, the energy and power are computed directly from the current and voltage time recordings and not from any particular electric model, which are believe to represent better the true performance of the device. The delivered energy density at current density of 500 µAcm^{-2} reaches 0.03 µWh cm^{-2} which is comparable to MXene/CNT (0.05 µWh cm^{-2} at 2 µAcm^{-2} [REF 8 from SI]) and MXene/CNF (0.08 µWh cm^{-2} at 570 µAcm^{-2} [REF 10 from SI]), but lower than the energy performance reported for other 2D materials-based devices (see Table 1S). This energy storage capability could be enhanced for instance by further increasing the deposition time and/or chemically or physically post-process the active material to increase its electrical conductivity. However, the power performance is outstanding with 1404 µW cm^{-2} at a constant current rate of 0.5 mA cm^{-2}, which is superior than most of the 2D materials-based devices (see Table 1S), such as MXene (2.4 µW cm^{-2} at 2 µA cm^{-2} for MXene/CNT [REF 8 in SI] or 145 µW cm^{-2} at 570 µA cm^{-2} for MXene/CNF [REF 10 in SI]), 2D MnO_2 (639 µW cm^{-2} at 500 µA cm^{-2} [REF 7 in SI]), and comparable to graphene (750 µW cm^{-2} at 20 mA cm^{-2} [REF 3 in SI]) and graphene oxide (1051 µW cm^{-2} at 1100 µA cm^{-2} [REF 11 in SI]). This high-rate energy delivery capability is in line with the CPE behaviour in the low-to-medium frequencies as reported in Figure 4(a). The results indicate that BP is a promising candidate for capacitive energy storage application.

Conclusion

In summary, in this research, a novel two-in-one exfoliation and deposition from bulk BP to phosphorene nanosheets were carried out for the first time via BPE method. In addition to the main advantage of this technique, which is the two-in-one exfoliation-and-deposition process, this method is proven to be simple, reliable, and eco-friendly. It is operated at ambient temperature in DI water without any chemical additives which makes it more attractive compared to previously reported electrochemical exfoliation approaches [75]. In principle, a large number of conductive substrates can be coated at once with this method using a single dc power supply without any Ohmic connection to the bipolar electrode, which could be positive attribute for scaling up purposes for different applications.

The high-quality exfoliated BP nanosheets were then analysed with different microscopic and spectroscopic techniques, revealing thin layers of phosphorene with orthorhombic crystal structure and lateral dimensions up to a few hundreds of nanometres. Furthermore, the electrochemical evaluation of the positive feeding electrode assembled in a symmetric configuration revealed a relatively acceptable discharge energy of 0.03 µWh cm^{-2} at a constant current load discharge of 500 µA cm^{-2} but with a very high rate of 1404 µW cm^{-2}. The device exhibited a fractional order capacitive behaviour in the low-to-medium frequency, and a high stability and reversibility for at least to 40000 cycles. We believe that this study could open up new horizons for the exfoliation and deposition of not only BP, but also other 2D materials for electronic and electrochemical energy storage device applications.

Conflict of interest

The authors declare no conflict of interest.

Acknowledgments

This work was partially supported by the US National Science Foundation awards 1506640, 1509735 and 1611088. The authors gratefully acknowledge Dr. Yusuf Emirov at the University of South Florida for his assistance in TEM analysis. The authors would like to thank the staff members of the Advanced Materials Engineering Research Institute (AMERI) and Dr. Andriy Durygin at the Center of the Study of Matter at Extreme Conditions (CeSMEC) at FIU in providing instrumentation assistance.

Notes and references

1. K. S. Novoselov, D. Jiang, F. Schedin, T. Booth, V. Khotkevich, S. Morozov and A. K. Geim, *Proc. Natl. Acad. Sci.*, 2005, **102**, 10451-10453.
2. S. Surnev, M. Ramsey and F. J. P. i. s. s. Netzer, *Prog. Surf. Sci.*, 2003, **73**, 117-165.
3. Q. H. Wang, K. Kalantar-Zadeh, A. Kis, J. N. Coleman and M. S. J. N. n. Strano, *Nat. Nanotechnol.*, 2012, **7**, 699.
4. D. Golberg, Y. Bando, Y. Huang, T. Terao, M. Mitome, C. Tang and C. J. A. n. Zhi, *ACS Nano*, 2010, **4**, 2979-2993.
5. K. S. Novoselov, V. Fal, L. Colombo, P. Gellert, M. Schwab and K. J. n. Kim, *Nature*, 2012, **490**, 192.

6. D. Akinwande, C. J. Brennan, J. S. Bunch, P. Egberts, J. R. Felts, H. Gao, R. Huang, J.-S. Kim, T. Li and Y. J. E. M. L. Li, *Extreme Mech. Lett.*, 2017, **13**, 42-77.
7. C. Zhu, D. Du and Y. J. D. M. Lin, *2D Mater.*, 2015, **2**, 032004.
8. J.-H. Chen, C. Jang, S. Xiao, M. Ishigami and M. S. J. N. n. Fuhrer, *Nat. Nanotechnol.*, 2008, **3**, 206.
9. T. Wang, Y. Zhu and Q. J. T. J. o. P. C. C. Jiang, *J Phys Chem C* 2013, **117**, 12873-12881.
10. H. Zhang, S. Lu, J. Zheng, J. Du, S. Wen, D. Tang and K. J. O. e. Loh, *Opt. Express*, 2014, **22**, 7249-7260.
11. P. J. J. o. t. A. C. S. Bridgman, *J. Am. Chem. Soc.*, 1916, **38**, 609-612.
12. X. Ling, H. Wang, S. Huang, F. Xia and M. S. J. P. o. t. N. A. o. S. Dresselhaus, *Proc. Natl. Acad. Sci. U. S. A.*, 2015, **112**, 4523-4530.
13. H. Liu, A. T. Neal, Z. Zhu, Z. Luo, X. Xu, D. Tománek and P. D. J. A. n. Ye, *ACS Nano*, 2014, **8**, 4033-4041.
14. H. Huang, B. Jiang, X. Zou, X. Zhao and L. J. S. B. Liao, *Sci. Bull.*, 2019.
15. X. Wang, A. M. Jones, K. L. Seyler, V. Tran, Y. Jia, H. Zhao, H. Wang, L. Yang, X. Xu and F. J. N. n. Xia, *Nat. Nanotechnol.*, 2015, **10**, 517.
16. X. Zhang, H. Xie, Z. Liu, C. Tan, Z. Luo, H. Li, J. Lin, L. Sun, W. Chen and Z. J. A. c. i. e. Xu, *Angew. Chem.*, 2015, **54**, 3653-3657.
17. S. Das, W. Zhang, M. Demarteau, A. Hoffmann, M. Dubey and A. J. N. l. Roelofs, *Nano Lett.*, 2014, **14**, 5733-5739.
18. F. Xia, H. Wang and Y. J. N. c. Jia, *Nat. Commun.*, 2014, **5**, 4458.
19. Q. Wei and X. J. A. P. L. Peng, *Appl. Phys. Lett.*, 2014, **104**, 251915.
20. V. Eswaraiah, Q. Zeng, Y. Long and Z. J. S. Liu, *Small*, 2016, **12**, 3480-3502.
21. C. Hao, B. Yang, F. Wen, J. Xiang, L. Li, W. Wang, Z. Zeng, B. Xu, Z. Zhao, Z. Liu and Y. Tian, *Adv. Mater.*, 2016, **28**, 3194-3201.
22. Z. Guo, W. Ding, X. Liu, Z. Sun and L. J. A. M. T. Wei, *Appl Mater Today.*, 2019, **14**, 51-58.
23. F. Xia, H. Wang, J. C. Hwang, A. C. Neto and L. Yang, *Nat. Rev. Physics*, 2019, 1.
24. R. Gusmao, Z. Sofer and M. J. A. C. I. E. Pumera, *Angew. Chem.*, 2017, **56**, 8052-8072.
25. Y. Zhang, Y. Zheng, K. Rui, H. H. Hng, K. Hippalgaonkar, J. Xu, W. Sun, J. Zhu, Q. Yan and W. Huang, *Small*, 2017, **13**, 1700661.
26. J. B. Smith, D. Hagaman and H.-F. Ji, *Nanotechnology*, 2016, **27**, 215602.
27. Z. Yang, J. Hao, S. Yuan, S. Lin, H. M. Yau, J. Dai and S. P. Lau, *Adv. Mater.*, 2015, **27**, 3748-3754.
28. L. Li, Y. Yu, G. J. Ye, Q. Ge, X. Ou, H. Wu, D. Feng, X. H. Chen and Y. J. N. n. Zhang, *Nat. Nanotechnol.*, 2014, **9**, 372.
29. S. Lin, Y. Chui, Y. Li and S. P. J. F. Lau, *FlatChem*, 2017, **2**, 15-37.
30. H. Wang, X. Yang, W. Shao, S. Chen, J. Xie, X. Zhang, J. Wang and Y. J. J. o. t. A. C. S. Xie, *J. Am. Chem. Soc.*, 2015, **137**, 11376-11382.
31. J. R. Brent, N. Savjani, E. A. Lewis, S. J. Haigh, D. J. Lewis and P. J. C. c. O'Brien, *Chem. Commun.*, 2014, **50**, 13338-13341.
32. C. Xing, J. Zhang, J. Jing, J. Li and F. Shi, *Chem. Eng. J.*, 2019.
33. Y. Zhang, H. Wang, Z. Luo, H. T. Tan, B. Li, S. Sun, Z. Li, Y. Zong, Z. J. Xu and Y. J. A. E. M. Yang, *Adv. Energy Mater.*, 2016, **6**, 1600453.
34. P. Yasaei, B. Kumar, T. Foroozan, C. Wang, M. Asadi, D. Tuschel, J. E. Indacochea, R. F. Klie and A. J. A. M. Salehi-Khojin, *Adv. Mater.*, 2015, **27**, 1887-1892.
35. S. Lin, Y. Li, W. Lu, Y. San Chui, L. Rogée, Q. Bao and S. P. J. D. M. Lau, *2D Mater.*, 2017, **4**, 025001.
36. W. Zhao, Z. Xue, J. Wang, J. Jiang, X. Zhao, T. J. A. a. m. Mu and interfaces, *ACS Appl. Mater. Interfaces*, 2015, **7**, 27608-27612.
37. D. Hanlon, C. Backes, E. Doherty, C. S. Cucinotta, N. C. Berner, C. Boland, K. Lee, A. Harvey, P. Lynch and Z. J. N. c. Gholamvand, *Nat. Commun.*, 2015, **6**, 8563.
38. Z. Yan, X. He, L. She, J. Sun, R. Jiang, H. Xu, F. Shi, Z. Lei and Z.-H. J. J. o. M. Liu, *J Materiomics*, 2018, **4**, 129-134.
39. A. Abdelkader, A. Cooper, R. Dryfe and I. J. N. Kinloch, *Nanoscale*, 2015, **7**, 6944-6956.
40. M. B. Erande, M. S. Pawar, D. J. J. A. a. m. Late and interfaces, *ACS Appl. Mater. Interfaces*, 2016, **8**, 11548-11556.
41. S. Qiu, B. Zou, H. Sheng, W. Guo, J. Wang, Y. Zhao, W. Wang, R. K. Yuen, Y. Kan, Y. J. A. a. m. Hu and interfaces, *ACS Appl. Mater. Interfaces*, 2019.
42. J. Li, C. Chen, S. Liu, J. Lu, W. P. Goh, H. Fang, Z. Qiu, B. Tian, Z. Chen and C. J. C. o. M. Yao, *Chem. Mater.*, 2018, **30**, 2742-2749.

43. A. Ambrosi, Z. Sofer and M. J. A. C. I. E. Pumera, *Angew. Chem.*, 2017, **56**, 10443-10445.
44. J. Backhurst, J. Coulson, F. Goodridge, R. Plimley and M. J. J. o. t. E. S. Fleischmann, *J. Electrochem. Soc.*, 1969, **116**, 1600-1607.
45. L. Koefoed, S. U. Pedersen and K. J. C. O. i. E. Daasbjerg, *Curr. Opin. Electrochem.*, 2017, **2**, 13-17.
46. S. E. Fosdick, K. N. Knust, K. Scida and R. M. J. A. C. I. E. Crooks, *Angew. Chem.*, 2013, **52**, 10438-10456.
47. G. Loget, D. Zigah, L. Bouffier, N. Sojic and A. J. A. o. c. r. Kuhn, *Acc. Chem. Res.*, 2013, **46**, 2513-2523.
48. A. Allagui, M. A. Abdelkareem, H. Alawadhi and A. S. J. S. r. Elwakil, *Sci. Rep.* , 2016, **6**, 21282.
49. A. Allagui, J. M. Ashraf, M. Khalil, M. A. Abdelkareem, A. S. Elwakil and H. J. C. Alawadhi, *ChemElectroChem*, 2017, **4**, 2084-2090.
50. I. Khakpour, A. Rabiei Baboukani, A. Allagui and C. Wang, *ACS Applied Energy Materials*, 2019, **2**, 4813-4820.
51. H. Hashimoto, Y. Muramatsu, Y. Nishina and H. Asoh, *Electrochemistry Communications*, 2019, **104**, 106475.
52. N. Mao, S. Zhang, J. Wu, J. Zhang and L. J. S. M. Tong, *Small Methods*, 2018, **2**, 1700409.
53. Z. Guo, H. Zhang, S. Lu, Z. Wang, S. Tang, J. Shao, Z. Sun, H. Xie, H. Wang and X. F. J. A. F. M. Yu, *Adv. Funct. Mater.*, 2015, **25**, 6996-7002.
54. A. Favron, E. Gaufrès, F. Fossard, A.-L. Phaneuf-L'Heureux, N. Y. Tang, P. L. Lévesque, A. Loiseau, R. Leonelli, S. Francoeur and R. J. N. m. Martel, *Nat. Mater.*, 2015, **14**, 826.
55. X. Ren, J. Zhou, X. Qi, Y. Liu, Z. Huang, Z. Li, Y. Ge, S. C. Dhanabalan, J. S. Ponraj and S. J. A. E. M. Wang, *Adv. Energy Mater.*, 2017, **7**, 1700396.
56. F. Luo, D. Wang, J. Zhang, X. Li, D. Liu, H. Li, M. Lu, X. Xie, L. Huang and W. J. A. A. N. M. Huang, *ACS Appl. Nano Mater.*, 2019.
57. A. Castellanos-Gomez, L. Vicarelli, E. Prada, J. O. Island, K. Narasimha-Acharya, S. I. Blanter, D. J. Groenendijk, M. Buscema, G. A. Steele and J. J. D. M. Alvarez, *2D Mater.*, 2014, **1**, 025001.
58. Y. Feng, J. Zhou, Y. Du, F. Miao, C.-G. Duan, B. Wang and X. J. J. o. P. C. M. Wan, *J. Phys.: Condens. Matter*, 2015, **27**, 185302.
59. J.-Y. Xu, L.-F. Gao, C.-X. Hu, Z.-Y. Zhu, M. Zhao, Q. Wang and H.-L. J. C. C. Zhang, *Chem. Commun.* , 2016, **52**, 8107-8110.
60. W. Lu, H. Nan, J. Hong, Y. Chen, C. Zhu, Z. Liang, X. Ma, Z. Ni, C. Jin and Z. Zhang, *Nano Research*, 2014, **7**, 853-859.
61. K. L. Kuntz, R. A. Wells, J. Hu, T. Yang, B. Dong, H. Guo, A. H. Woomer, D. L. Druffel, A. Alabanza, D. J. A. a. m. Tománek and interfaces, *ACS Appl. Mater. Interfaces*, 2017, **9**, 9126-9135.
62. H. Xiao, M. Zhao, J. Zhang, X. Ma, J. Zhang, T. Hu, T. Tang, J. Jia and H. Wu, *Electrochemistry Communications*, 2018, **89**, 10-13.
63. Z. Sun, Y. Zhang, H. Yu, C. Yan, Y. Liu, S. Hong, H. Tao, A. W. Robertson, Z. Wang and A. A. Pádua, *Nanoscale*, 2018, **10**, 12543-12553.
64. D. J. J. M. Late and M. Materials, *Microporous Mesoporous Mater.*, 2016, **225**, 494-503.
65. J. Kang, J. D. Wood, S. A. Wells, J.-H. Lee, X. Liu, K.-S. Chen and M. C. J. A. n. Hersam, *ACS Nano*, 2015, **9**, 3596-3604.
66. M. Fouda, A. Elwakil, A. Radwan and A. Allagui, *Energy*, 2016, **111**, 785-792.
67. A. Allagui, D. Zhang and A. S. Elwakil, *Appl. Phys. Lett.*, 2018, **113**, 253901.
68. A. Allagui, T. J. Freeborn, A. S. Elwakil, M. E. Fouda, B. J. Maundy, A. G. Radwan, Z. Said and M. A. J. J. o. P. S. Abdelkareem, *J. Power Sources*, 2018, **400**, 457-467.
69. A. Allagui, T. J. Freeborn, A. S. Elwakil and B. J. J. S. r. Maundy, *Sci. Rep.* , 2016, **6**, 38568.
70. I. J. I. T. o. a. c. Podlubny, *IEEE Trans. Autom. Control*, 1999, **44**, 208-214.
71. A. G. Radwan, A. Shamim, K. N. J. I. M. Salama and W. C. Letters, *IEEE Microw. Wireless Compon. Lett*, 2011, **21**, 120-122.
72. A. S. J. I. C. Elwakil and S. Magazine, *IEEE Circuits Syst Mag.*, 2010, **10**, 40-50.
73. M. E. Fouda, A. Allagui, A. S. Elwakil, A. Eltawil and F. Kurdahi, *Journal of Power Sources*, 2019, **435**, 226829.
74. M. E. Fouda, A. Allagui, A. S. Elwakil, A. Eltawil and F. J. J. o. P. S. Kurdahi, *J. Power Sources*, 2019, **435**, 226829.
75. A. Ambrosi and M. J. C. S. R. Pumera, *Chem. Soc. Rev.*, 2018, **47**, 7213-7224.